

Calibration of a general analytical model for the debonding strength of NSM-CFRP strip-concrete joints using particle swarm optimization

Sila Yaman ^{*,a}

Department of Civil Engineering, Süleyman Demirel University, Isparta, Türkiye

Article Info

Abstract

Article History:

Received 05 Sep 2025

Accepted 25 Sep 2025

Keywords:

Intermediate crack (IC)
debonding;
Particle swarm
optimization;
NSM;
CFRP strip

The use of FRP composites in the strengthening of existing structures has become increasingly common. In the strengthening of reinforced concrete (RC) elements using FRP through either the externally bonded reinforcement (EBR) or near-surface mounted (NSM) methods, the interface between the FRP and the concrete is typically the weakest link, which negatively affects the overall effectiveness of the strengthening technique. One of the primary damage mechanisms observed in RC members strengthened with NSM-CFRP strips is intermediate crack (IC) debonding. To estimate the maximum debonding resistance that develops in the NSM-CFRP strip against this type of failure, an existing analytical model in the literature was recalibrated using Particle Swarm Optimization (PSO). While preserving the original functional form proposed by the authors, four separate models were developed. The resulting coefficients and performance metrics (RMSE, MAE) were then compared with those of the existing model, which uses fixed coefficients reported in the literature, based on the same dataset. The recalibrated model achieved 6.9% improvement in MAE, demonstrating better prediction accuracy and more consistent performance across individual runs. These improvements can contribute to more efficient and reliable FRP strengthening designs by improving the accuracy of debonding strength estimation and enhancing economical design.

© 2025 MIM Research Group. All rights reserved.

1. Introduction

As reinforced concrete (RC) structures are exposed to increasing load demands or design deficiencies, their structural performance may gradually deteriorate. In such cases, strengthening techniques may become necessary to restore or enhance the load-carrying capacity, stiffness, or ductility - particularly to extend service life and improve safety under seismic or heavy loading conditions [1].

Recently, the use of Fiber Reinforced Polymer (FRP) composite materials in the strengthening of reinforced concrete (RC) structures has become increasingly widespread. There are two commonly adopted techniques for strengthening RC elements using composite materials: Externally Bonded Reinforcement (EBR) and Near Surface Mounted (NSM) methods [2-3]. In the EBR technique, FRP composites are bonded externally to the surface of the structural element, whereas in the NSM technique, FRP composites are embedded into grooves cut into the concrete cover and bonded using adhesives such as epoxy or repair mortars.

FRP composites are available in various forms, such as sheets, bars, and fabrics, and can be manufactured using different constituent materials, including carbon, glass, and aramid fibers.

^{*}Corresponding author: silayaman@sdu.edu.tr

^aorcid.org/0000-0003-3131-1090

DOI: <https://dx.doi.org/10.17515/resm2025-1131an0905rs>

Res. Eng. Struct. Mat. Vol. x Iss. x (xxxx) xx-xx

Among these, Carbon Fiber Reinforced Polymer (CFRP) composites are the most widely used type. Compared to other types such as GFRP and AFRP, CFRP composites are preferred in structural strengthening applications due to their high tensile strength and stiffness, lower unit weight, resistance to corrosion, favorable performance under fire exposure, better fatigue performance, and more advanced manufacturing technologies. FRP materials exhibit linear elastic behavior up to their ultimate tensile strength, beyond which they fail abruptly and lose their load-carrying capacity.

In any strengthening application, it is ideal to fully utilize the mechanical properties of the FRP material [4]. In RC elements strengthened with FRP, the interface between the FRP and concrete is often the weakest link, and this interface plays a critical role in determining the effectiveness of the strengthening technique [5]. One of the major failure modes observed in elements strengthened with NSM-CFRP strips is known as intermediate crack (IC) debonding [6–8]. This failure typically occurs when a flexural or tensile crack in the concrete intersects the bonded CFRP strip. At the intersection point, cracks initiate at the FRP–concrete interface and often propagate into the surrounding concrete substrate [6]. If these interface cracks coalesce and reach the end of the CFRP strip, the deformation in the strip decreases significantly, leading to what is defined as "intermediate crack debonding" (IC debonding) [6, 9] (Fig. 1).

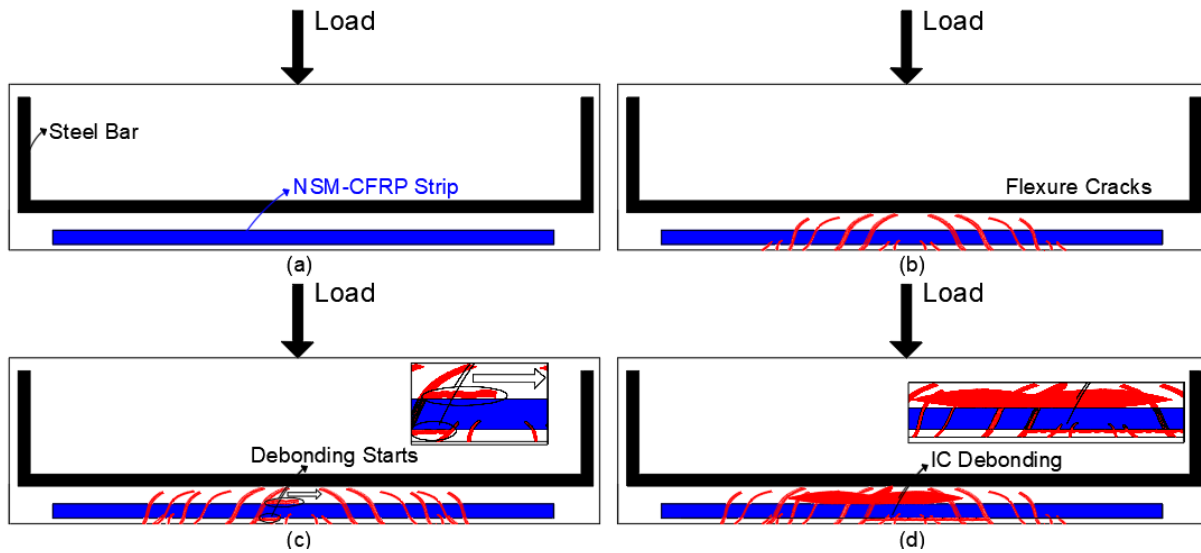


Fig. 1. Schematic illustration of the IC debonding failure mechanism (a) Initial state with applied load, (b) Development of flexural cracks intersecting the CFRP strip, (c) Initiation of debonding at the NSM-CFRP strip–concrete interface, (d) Propagation and coalescence of cracks leading to IC debonding failure

Several analytical models have been proposed in the literature to estimate the debonding strength at the NSM-CFRP interface, based on experimental studies [6, 10–17]. However, these models were generally calibrated using a limited number of experimental datasets. In the present study, the objective is to improve the accuracy of the model developed by Seracino et al. [6] by recalibrating its fixed parameters using Particle Swarm Optimization (PSO).

In recent years, the use of soft computing-based innovative approaches for solving civil engineering problems has been increasingly adopted [18–21]. In this context, artificial neural networks (ANNs) and/or machine learning (ML) techniques have been employed in various studies to predict or estimate key structural parameters, such as the compressive strength of concrete [22–24], the shear strength of reinforced concrete (RC) beams [25], the load-bearing capacity of strengthened RC slabs [26–27], and the required number of FRP layers for strengthening RC members or frames [28–29].

Li et al. [30] and Hu et al. [31] developed backpropagation neural network models to improve the accuracy of predicting debonding deformations in RC beams strengthened with FRP. Ghaidan et al. [32] applied multinomial logistic regression analysis to address the issue of concrete cover

separation - a premature failure mode observed in RC beams strengthened using NSM-FRP techniques.

Several studies in the literature have utilized Particle Swarm Optimization (PSO) for various structural engineering applications [33–34]. Ghodousian et al. [35] employed PSO to evaluate the interfacial bond strength of colored self-compacting concrete repair overlays. Mohammadzadeh and Esfandnia [36], as well as Wahab et al. [37], applied various metaheuristic algorithms, including PSO, to predict the compressive strength of reinforced concrete (RC) columns confined with FRP.

Nguyen and Lý [38] used Adaptive Neuro-Fuzzy Inference System (ANFIS) combined with PSO to estimate the bond strength between CFRP and concrete. Su et al. [39] proposed a backpropagation neural network model to predict the bond capacity at the NSM-CFRP-to-concrete interface. Kumar et al. [40] predicted the bond strength between FRP and concrete surfaces using Artificial Neural Networks (ANN), an optimized Artificial Bee Colony (ABC)-ANN, and Gaussian Process Regression (GPR). In a subsequent study, Kumar et al. [41] employed a PSO-optimized ANN approach. Pei and Wei [42] estimated this bond strength through an ant colony optimization-based ANFIS model. Zhang et al. [43] utilized six different ANN models. These models predict bond strength and shear capacity at the FRP-concrete interface. Tao and Xue [44] proposed a novel hybrid model. It integrates PSO with Random Forest (RF) techniques to predict FRP-concrete bond strength. Shbeeb et al. [45] applied both ANN and ANFIS methods. Xue et al. [46] validated the predictive capability of Multivariate Adaptive Regression Splines (MARS) and Wavelet Neural Network (WNN) algorithms for FRP-concrete bond strength. They also recalibrated these models using PSO. Moreover, Haddad et al. [47] employed artificial neural networks to determine the bond strength between EBR-FRP and heat-damaged concrete.

There are numerous studies in the literature predicting the debonding strength at the NSM-CFRP and concrete interface using artificial intelligence and optimization algorithms. However, research focusing on systematic improvement of existing analytical models through recalibration using methods such as Particle Swarm Optimization (PSO) remains limited. This study aims to improve the predictive accuracy of an existing analytical model [6] used to estimate the debonding strength at the NSM-CFRP strip-concrete interface. To this end, while preserving the original mathematical structure of the model, its constant coefficients were recalibrated using the Particle Swarm Optimization (PSO) technique. By adapting the model - originally proposed in the literature with fixed coefficients - to the available dataset through optimization, its prediction performance has been enhanced. During the calibration process, Root Mean Square Error (RMSE) and Mean Absolute Error (MAE) were used as cost functions, and two scenarios were considered: one with the first two geometric coefficients fixed, and one with them included as variables. As a result of the calibration, improvements of 0.73% in RMSE and 6.9% in MAE were achieved. Although these numerical differences may appear small, they can contribute to the design of CFRP-strengthened structures in a safer, more economical manner - avoiding unnecessary conservatism. In this respect, the study brings data-driven refinement to existing analytical models and enables more accurate predictions in structural engineering applications.

2. Material and Method

2.1. Material

Seracino et al. [6] proposed an analytical model to predict the debonding strength at the NSM CFRP strip - concrete interface using experimental data compiled from the literature. In the present study, the same experimental dataset was used to recalibrate the analytical model through the Particle Swarm Optimization (PSO) method. The experiments were conducted on CFRP strips embedded into concrete blocks using the NSM technique, and debonding strengths were obtained under push-pull loading conditions. The loading was uniaxial and applied in a monotonic (continuously increasing) manner. In the tested specimens, key parameters such as CFRP strip width (d_p), thickness (b_p), elastic modulus (E_p), embedment length (L), and concrete compressive strength (f_c) were varied. The ranges of these parameters are as follows: strip width (d_p), 9.95 - 20.47 mm; strip thickness (b_p), 1.2 - 2.9 mm; elastic modulus (E_p), 144600 - 162300 MPa; embedment length (L), 200 - 350 mm and concrete compressive strength (f_c): 30 - 65 MPa. These

parameters are the key factors influencing the debonding behavior at the NSM-CFRP interface and are critical for the calibration and validation of the model. The dataset used in this study consists of a total of 21 experimental tests, covering various combinations of the listed parameters. Statistical information related to these parameters and the corresponding experimental debonding strength results (P_{exp}) is provided in Table 1.

Table 1. Statistical data of the experimental dataset used in the study

	d_p (mm)	b_p (mm)	E_p (MPa)	f_c (MPa)	L (mm)	P_{exp} (kN)
Mean	14.51	1.33	161,195.24	43.48	233.33	47.63
Standard Error	1.03	0.08	831.36	2.51	11.09	4.14
Median	10.56	1.26	161,800.00	50.00	200.00	45.10
Standard Deviation	4.71	0.36	3809.75	11.52	50.83	18.97
Sample Variance	22.21	0.13	14,514,226.19	132.66	2583.33	359.83
Kurtosis	-1.97	20.76	20.81	-1.45	-0.46	-1.54
Skewness	0.30	4.54	-4.55	-0.12	1.08	0.33
Range	10.52	1.70	17,700.00	35.00	150.00	54.90
Minimum	9.95	1.20	144,600.00	30.00	200.00	23.00
Maximum	20.47	2.90	162,300.00	65.00	350.00	77.90
Sample Size	21					

2.2. Method

2.1.1 Analytical Model for Debonding Strength

Seracino et al. [6] proposed a generalized analytical model to predict the interfacial debonding strength (P_{IC}) of adhesively bonded strip-concrete interfaces. The model was developed by considering an idealized bond-slip relationship of the strip-concrete interface. It is a practical model applicable to strips used in both Externally Bonded Reinforcement (EBR) and Near Surface Mounted (NSM) techniques, and it depends solely on the strip geometry and material properties. The maximum debonding strength at the strip-concrete interface is expressed by Eq (1):

$$P_{IC} = \sqrt{\tau_{max} \times \delta_{max}} \cdot \sqrt{L_{per} \times E_p \times A_p} \quad (1)$$

$$L_{per} = 2d_f + b_f \quad (2)$$

$$d_f = d_p + t_d, \quad b_f = b_p + 2t_b \quad (t_d = t_b = 1) \quad (3)$$

$$A_p = b_p \times d_p \quad (4)$$

Fig. 2 schematically illustrates the debonding failure plane that occurs at strip-to-concrete interfaces and forms the conceptual foundation of the modeling approach adopted in this study. The debonding surface is defined as the mortar layer that separates from the concrete substrate while remaining attached to the CFRP strip. The transverse and longitudinal thicknesses of the mortar layer adhered to the strip are denoted as t_b and t_d , respectively. In the model proposed by Seracino et al. [6], these thicknesses are assumed to be constant and equal to 1 mm. The debonding surface is represented as a rectangular failure region characterized by its width (b_f) and depth (d_f), which are geometrically related to the dimensions of the NSM CFRP strip (b_p and d_p). The parameter L_{per} denotes the effective debonding length in the transverse section and plays a significant role in the transfer of shear stress along the interface. In this context, δ_{max} represents the maximum slip displacement that occurs at the interface prior to complete debonding, while τ_{max} denotes the corresponding maximum shear stress. Together, these two quantities define the energy dissipation capacity of the interface ($\tau_{max} \times \delta_{max}$), which is modeled as a function of the aspect ratio (ϕ_f) of the failure plane and the cylindrical compressive strength of concrete (f_c), as shown in Eq (5) and Eq (6). As illustrated in Fig. 2, this modeling approach assumes that debonding occurs along a well-

defined shear plane, the geometry of which governs the mechanical behavior of the bonded joint. Therefore, Fig. 2 not only serves as a conceptual basis for the analytical model but also helps visualize the physical meaning of the key parameters involved in the calibration process.

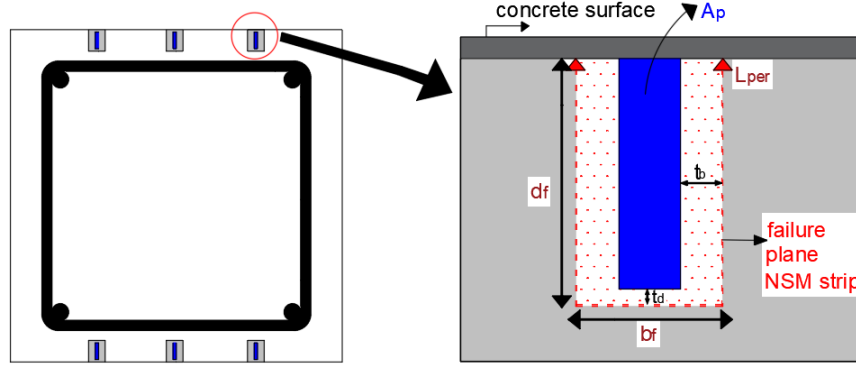


Fig. 2. IC Debonding failure plane of the strip embedded in the groove ($t_b = t_d = 1 \text{ mm}$) [6]

$$\varphi_f = \frac{d_f}{b_f} \quad (5)$$

$$\delta_{max} \times \tau_{max} = (C \times \varphi_f^m \times f_c^n) \quad (6)$$

Here, the constants C , m , and n were optimized using linear regression analysis. The values of δ_{max} and τ_{max} , which are necessary for determining the debonding strength, were obtained using Eq (7) and Eq (8), respectively.

$$\tau_{max} = (0.802 + 0.078\varphi_f) \times f_c^{0.6} \quad (7)$$

$$\delta_{max} = \frac{0.976\varphi_f^{0.526}}{0.802 + 0.078\varphi_f} \quad (8)$$

In the proposed analytical model for determining the debonding strength, the values of t_b and t_d are assumed to be constant and equal to one, as stated in the study. Accordingly, by modifying Eq (3), an expression containing constant coefficients is obtained (Eq 9).

$$d_f = d_p + 1, \quad b_f = b_p + 2 \quad (9)$$

Within the scope of this study, the calibration of the constant values in the analytical model (1 and 2 due to t_b and t_d ; 0.976, 0.526, 0.802, 0.078, and 0.6) was performed using Particle Swarm Optimization (PSO). Since these values were originally treated as fixed coefficients in the model equations, they were redefined as variable parameters (K_1, K_2, \dots, K_7) in the optimization process. This allowed the PSO algorithm to iteratively update their values during each run in order to identify the optimal set of coefficients. Based on the original analytical formulation and the parameters described above, the modified model used in the optimization process is expressed in Eq 10. In this equation, the constants are replaced by optimization variables (K_1 to K_7) to allow for calibration using PSO:

$$P_{IC} = \sqrt{\left(\left(k_5 + k_6 \left(\frac{d_p + k_1}{b_p + k_2} \right) \right) \cdot f_c^{k_7} \right) \cdot \left(\frac{k_3 \left(\frac{d_p + k_1}{b_p + k_2} \right)^{k_4}}{\left(k_5 + k_6 \left(\frac{d_p + k_1}{b_p + k_2} \right) \right)} \right) \cdot \sqrt{[2(d_p + k_1) + (b_p + k_2)] \cdot E_p \cdot (d_p \cdot b_p)}} \quad (10)$$

Table 2 presents the mapping between the parameters used in the PSO algorithm and their corresponding constants in the analytical model.

Table 2. Constants used in the model

PSO Parameter	K ₁	K ₂	K ₃	K ₄	K ₅	K ₆	K ₇
Original Constant	1	2	0.976	0.526	0.802	0.078	0.6
Equation Number	Eq 9	Eq 9	Eq 8	Eq 8	Eq 7, Eq 8	Eq 7, Eq 8	Eq 7

K₁ and K₂ are geometric correction coefficients affecting the interaction area between the CFRP strip and concrete (related to the adhesive thickness and width). They replace the constants 1 and 2 in Eq 9. K₃ and K₄ represent the multiplier and exponent parameters used in the function defining the maximum shear displacement, which governs the deformation characteristics of the interface. K These replace the constants 0.976 and 0.526 in Eq 8. K₅ and K₆ are linear coefficients associated with ϕ_f in the maximum shear stress formula. They replace the values 0.802 and 0.078 in Eq 7 and Eq 8, respectively. K₇ is the exponential parameter reflecting the influence of concrete compressive strength and replaces the value 0.6 in Eq 7. These parameters are directly integrated into the mathematical formulation of the model and are optimized to enhance prediction accuracy.

2.2.2 Partical Swarm Optimization

Particle Swarm Optimization (PSO) is a nature-inspired metaheuristic optimization algorithm developed by Kennedy and Eberhart in 1995 [48]. The fundamental inspiration behind the algorithm is the collective behavior exhibited by flocks of birds or schools of fish while searching for food. Based on swarm intelligence, this algorithm is simple yet powerful [49–50]. PSO is widely used to solve nonlinear and complex problems in continuous or discrete parameter spaces.

PSO operates on a swarm consisting of individuals called "particles," which represent a set of potential solutions. Each particle corresponds to a point in the solution space and possesses certain velocity and position information. Over time, these particles move toward better solutions by learning from their own experiences as well as the best experiences of other particles in the swarm [51]. Fundamentally, PSO relies on particles adjusting their positions toward the best position found by any member of the swarm, and this process continues iteratively until the target is achieved [52]. The flowchart illustrating the steps of the algorithm is presented in Fig. 3.

In PSO, the initial position (Eq 11) and velocity (Eq 12) of each particle are first determined [53]. The fitness values of each particle, which lie within the defined boundary limits, are then calculated using Eq (13). In each iteration, the personal best (p_{best}) values - representing the best solution a particle has found so far - and the global best (g_{best}) values - representing the best solution found by any particle in the entire population - are identified. Based on these two best values, the velocities (Eq 14) and positions (Eq 15) of the particles are updated accordingly.

$$\begin{bmatrix} X_{11} & X_{12} & \dots & X_{1n} \\ \vdots & \vdots & \dots & \vdots \\ X_{m1} & X_{m2} & \dots & X_{mn} \end{bmatrix} \quad (11)$$

$$\begin{bmatrix} V_{11} & V_{12} & \dots & V_{1n} \\ \vdots & \vdots & \dots & \vdots \\ V_{m1} & V_{m2} & \dots & V_{mn} \end{bmatrix} \quad (12)$$

$$\begin{bmatrix} f(1) = f(X_{11}, X_{12}, \dots X_{1n}) \\ \vdots \\ f(m) = f(X_{m1}, X_{m2}, \dots X_{mn}) \end{bmatrix} \quad (13)$$

$$V_{id} = W V_{id} + c_1 rand_1(pbest_{id} - X_{id}) + c_2 rand_2(gbest - X_{id}) \quad (14)$$

$$X_{id} = X_{id} + V_{id} \quad (15)$$

Here, W represents the inertia weight; c_1 and c_2 are the acceleration (or scaling) coefficients; X_{id} denotes the position, and V_{id} denotes the velocity of the particle. The terms $rand_1$ and $rand_2$ are uniformly distributed random numbers between [0–1]. For problems with fewer parameters and low complexity, a larger inertia weight value may be used, whereas for more complex problems, a smaller value is generally preferred [54].

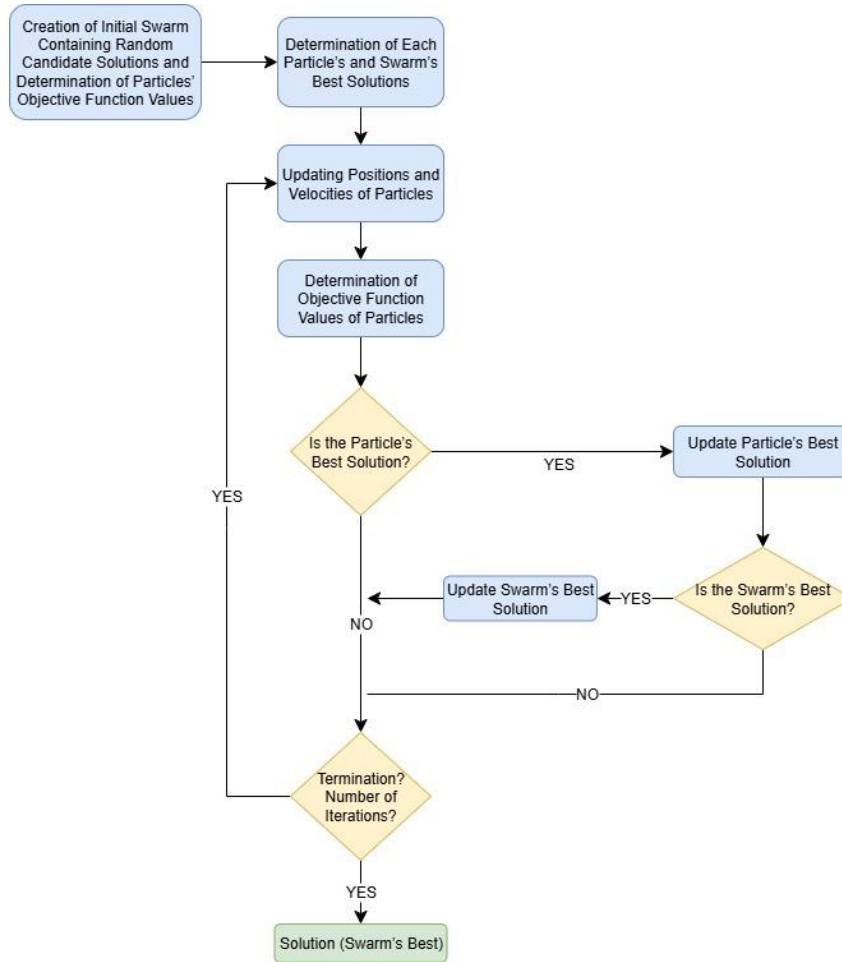


Fig. 3. Flowchart of the PSO algorithm [50]

To effectively operate the Particle Swarm Optimization (PSO) algorithm, an objective function is required to evaluate the performance of each possible parameter combination within the solution space. In this study, a PSO-based model was developed with the aim of modifying the constants in the analytical model proposed by Seracino et al. [6] to achieve results that more closely match the experimental data. The inertia weight (W) was set to 0.7. The cognitive (c_1) and social (c_2) acceleration coefficients were taken as 1.5. The swarm size (m) was fixed at 30 particles, and the maximum number of iterations was limited to 1000.

Two different error metrics were used to evaluate the predictive performance of the model: Mean Absolute Error (MAE) and Root Mean Square Error (RMSE). These error metrics are calculated based on the differences (i.e., errors) between the maximum load predicted by the PSO-calibrated model and the experimentally obtained load values.

2.2.3 Root Mean Square Error (RMSE)

RMSE is the square root of the mean of the squared errors. Since it involves squaring the errors, it penalizes larger errors more heavily.

$$RMSE = \sqrt{\frac{1}{n} \sum_{i=1}^n (P_i - P'_i)^2} \quad (16)$$

2.2.4 Mean Absolute Error (MAE)

MAE is the mean of the absolute values of the errors. It directly reflects the magnitude of the model's prediction errors and treats all errors equally, regardless of their direction or size.

$$MAE = \frac{1}{n} \sum_{i=1}^n |P_i - P'_i| \quad (17)$$

In both error metrics, values approaching zero indicate higher model accuracy. While MAE provides a general measure of the average error magnitude, RMSE reflects the model's sensitivity to larger deviations. In this study, RMSE and MAE were used as objective functions in the optimization process, and the aim was to identify the set of coefficients that minimize these error metrics.

2.2.5 Model Calibration

In this study, the original formula structure was preserved, and all models were calibrated using Particle Swarm Optimization (PSO). The general procedure involved in putting the data, running PSO with random initializations, calculating the selected error metric for each candidate coefficient set at every iteration, retaining the coefficient set with the minimum error, and outputting the best coefficients once the stopping criteria were met (Fig. 4).

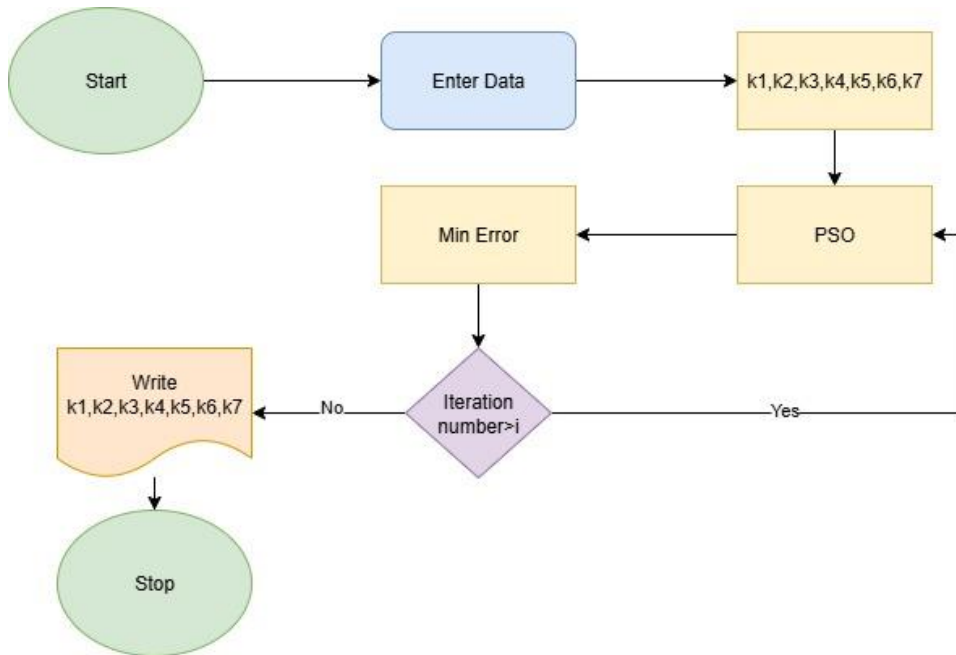


Fig. 4. Flowchart of the model calibration process

In this study, the termination criterion of the PSO algorithm was defined as reaching the maximum number of iterations. The error value was monitored by the decision-maker to evaluate the quality of the obtained solutions; however, no automatic error-based stopping condition was applied. PSO parameters remained consistent across all models to ensure that the comparison was based on the choice of error metric and the status of the first two coefficients. The optimization target was the "P_{IC}" value, which corresponds to the expression originally defined in Eq 1 and reformulated in Eq 10 for optimization purposes.

In the first model, the objective is to minimize the error according to the RMSE criterion. To ensure compatibility with the literature, K₁ and K₂ are kept fixed; PSO searches only over K₃ to K₇. In the flowchart, this is represented by the "PSO" block operating on a parameter set and the "Min Error = RMSE" evaluation. The second model also focuses on RMSE but allows K₁ and K₂ to be free parameters. Thus, PSO searches across all K₁ to K₇, enabling an independent investigation of the effect of including the first two coefficients in the calibration. The flow remains the same; only the dimension of decision variables increases. In the third model, the error criterion is selected as MAE. To maintain comparability with the literature, K₁ and K₂ are fixed; PSO works on K₃ to K₇. The difference in the flowchart is that the error is calculated as MAE in the "Min Error" step. Other steps remain unchanged. The fourth model uses MAE as the error criterion and also includes k₁ and k₂ in

the calibration; PSO optimizes all coefficients from K_1 to K_7 . Thus, the effect of fixing or calibrating the first two coefficients on the MAE side is examined symmetrically alongside the RMSE side.

The software setup is consistent across all models. Each model is run with five independent trials; the best, average, and standard deviation values obtained in each trial were recorded for later reporting. Comparisons will be made along the axes of error metric selection (RMSE/MAE) and the status of coefficients K_1 and K_2 (fixed/free).

3. Results and Discussion

In this study, four models were developed using the same formula structure and all calibrated via Particle Swarm Optimization (PSO) models with fixed parameters $K_1 = 1$ and $K_2 = 2$, and free models where these two coefficients were also included in the calibration process. Regarding the error criterion, two models were optimized based on RMSE and two models based on MAE. The PSO search settings were kept constant throughout all experiments. Each model was run with five independent trials using different random initializations, and for each trial, the best (minimum), average, and standard deviation of the error values were reported (Table 3).

Table 3. Results of PSO analysis

Model	Independent Runs	K_1	K_2	K_3	K_4	K_5	K_6	K_7	RMSE	MAE
Model 1 K_1 - K_2 fixed, optimized based on RMSE	1.	1.000	2.000	0.845	0.537	0.521	0.467	0.633	0.274	
	2.	1.000	2.000	0.845	0.537	0.462	0.761	0.633	0.274	
	3.	1.000	2.000	0.845	0.537	0.379	0.652	0.633	0.274	
	4.	1.000	2.000	0.845	0.537	0.610	0.613	0.633	0.274	
	5.	1.000	2.000	0.845	0.537	0.415	0.495	0.633	0.274	
	Standard Deviation	0.000	0.000	0.000	0.000	0.090	0.119	0.000	0.000	
	Mean	1.000	2.000	0.845	0.537	0.477	0.598	0.633	0.274	
Model 2 7- variable, optimized based on RMSE	1.	0.500	2.261	0.983	0.510	0.429	0.669	0.625	0.273	
	2.	0.500	2.312	0.988	0.512	0.271	0.496	0.624	0.273	
	3.	0.501	2.274	0.984	0.510	0.867	0.600	0.625	0.273	
	4.	0.500	2.161	0.975	0.505	0.325	0.844	0.626	0.273	
	5.	0.500	2.284	0.987	0.510	0.323	0.542	0.624	0.273	
	Standard Deviation	0.000	0.054	0.005	0.003	0.244	0.122	0.001	0.000	
	Mean	0.500	2.258	0.983	0.509	0.443	0.630	0.625	0.273	
Model 3 K_1 - K_2 fixed, optimized based on MAE	1.	1.000	2.000	0.585	0.565	0.759	0.390	0.714		0.054
	2.	1.000	2.000	0.604	0.562	0.764	0.259	0.707		0.054
	3.	1.000	2.000	0.583	0.566	0.458	0.506	0.715		0.054
	4.	1.000	2.000	0.577	0.569	0.524	0.297	0.717		0.054
	5.	1.000	2.000	0.587	0.565	0.572	0.698	0.714		0.054
	Standard Deviation	0.000	0.000	0.010	0.003	0.138	0.163	0.004		0.000
	Mean	1.000	2.000	0.587	0.565	0.615	0.430	0.713		0.054
Model 4 7-variable, optimized based on MAE	1.	0.500	2.261	0.983	0.510	0.429	0.669	0.625		0.054
	2.	0.500	2.312	0.988	0.512	0.271	0.496	0.624		0.054
	3.	0.501	2.274	0.984	0.510	0.867	0.600	0.625		0.054
	4.	0.500	2.161	0.975	0.505	0.325	0.844	0.626		0.054
	5.	0.500	2.284	0.987	0.510	0.323	0.542	0.624		0.054
	Standard Deviation	0.000	0.054	0.005	0.003	0.244	0.122	0.001		0.000
	Mean	0.500	2.258	0.983	0.509	0.443	0.630	0.625		0.054
Coefficient from Literature	6.	1.000	2.000	0.976	0.526	0.802	0.078	0.600	0.275	0.058

The convergence consistency of the PSO runs was evaluated by analyzing the means and standard deviations of the coefficients (K_1 - K_7) and the error values obtained from the five independent runs for each model. Overall, all four models demonstrated strong convergence stability, with most

coefficients and error metrics exhibiting near-zero standard deviations. In Model 1, K_1 – K_4 and K_7 were highly stable, while K_5 (std ≈ 0.090) and K_6 (std ≈ 0.119) showed relatively higher variability. In Models 2 and 4, K_2 (std ≈ 0.054) and especially K_5 (std ≈ 0.244) displayed greater fluctuations, while the other parameters and error metrics remained consistent. In Model 3, K_3 and K_4 converged almost perfectly, with only K_5 (std ≈ 0.138) showing minor variability. The negligible variation in RMSE and MAE across all models confirms the reliability and reproducibility of PSO-based calibration. The obtained performance results and coefficient sets were compared with the existing method in the literature and its fixed coefficients, with the RMSE and MAE values of the reference method on the same dataset also presented. This approach clearly highlights the effects of treating the first two coefficients as adjustable and the choice of optimization criterion (RMSE/MAE).

Each of the four models was run using PSO with 5 independent trials, and the results were evaluated according to the model type using either RMSE or MAE. In the models optimized based on RMSE, the model with fixed K_1 and K_2 (RMSE–Fixed) consistently produced an RMSE of 0.274 across all trials, whereas the model with K_1 and K_2 treated as adjustable parameters (RMSE–Free) achieved an RMSE of 0.273 in every trial. This indicates that including K_1 and K_2 in the calibration yielded a small but consistent improvement of approximately 0.36% in RMSE. For the models optimized according to MAE, both the MAE–Fixed and MAE–Free models maintained a constant MAE value of 0.054 across all trials, suggesting that allowing K_1 and K_2 to vary did not provide any additional benefit within the reported precision for MAE. Although the coefficients in the models with adjustable parameters (particularly K_1 – K_6) showed some variability across the five independent trials, the optimized error metrics (RMSE and MAE) remained highly consistent, with minimum, mean, and standard deviation values nearly identical. Given that the metrics did not vary over the 5 trials (min = mean = std ≈ 0), it can be concluded that PSO converged reliably for this problem. While parameter standard deviations are generally low, some degree of correlation among parameters may exist, which is common in multi-parameter calibrations. This likely contributes to the consistent error metrics despite small parameter variations. Overall, the results indicate reliable and reproducible convergence of the PSO algorithm. Examining the parameter patterns reveals that in the RMSE–Fixed model (with $K_1 = 1$ and $K_2 = 2$), the coefficients K_5 and K_6 were mainly adjusted between trials, whereas in the RMSE–Free model, K_1 converged around 0.500 and K_2 ranged approximately between 2.16 and 2.31. This suggests that setting the first two coefficients as adjustable redefined the equilibrium among the remaining coefficients (e.g., K_5 and K_6) and led to a slight reduction in RMSE. In the MAE group, the MAE–Fixed model highlighted bands of $K_3 \approx 0.58 - 0.60$ and $K_4 \approx 0.56 - 0.57$, while in the MAE–Free model, K_1 and K_2 again converged to similar ranges as in the RMSE–Free model, despite the MAE value remaining constant. This indicates that the MAE metric, which is more robust against outliers, did not reflect performance gains from allowing K_1 and K_2 to vary, whereas RMSE, being more sensitive to larger errors, showed a small but positive effect. In summary, treating K_1 and K_2 as adjustable parameters provided a marginal but consistent improvement in RMSE, while no significant difference was observed based on MAE.

When compared to the literature method coefficients ($K_1 = 1$, $K_2 = 2$, $K_3 = 0.976$, $K_4 = 0.526$, $K_5 = 0.802$, $K_6 = 0.078$, $K_7 = 0.600$) and performance values (RMSE = 0.275, MAE = 0.058), the PSO-based models demonstrated improvements: the RMSE–Fixed model reduced RMSE to 0.274, achieving approximately a 0.36% improvement, while the RMSE–Free model further reduced RMSE to 0.273, corresponding to about a 0.73% enhancement. For the MAE-focused models, both fixed and flexible cases resulted in an MAE of 0.054, representing a roughly 6.9% decrease compared to the literature. In other words, treating K_1 and K_2 as adjustable parameters produced a small but consistent additional gain in RMSE, whereas the MAE remained unchanged.

The 6.9% reduction in MAE indicates a significant improvement in the overall accuracy and consistency of the model, which is particularly advantageous when generalizing to different structural configurations. This enhancement contributes to more reliable safety assessments, reduced overdesign, and improved efficiency in the use of strengthening materials such as CFRP. These aspects highlight the practical engineering relevance of the improvements achieved through the proposed recalibration approach.

The prediction results obtained using the model parameters that showed the best performance through the PSO method are compared with the experimental data and presented in Fig. 5. The proximity of the data points to the linear reference line indicates the success of the calibration and that the model provides results closer to the experimental values.

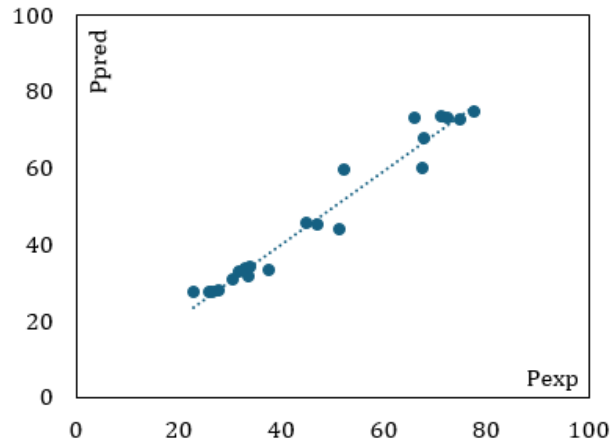


Fig. 5. Scatter plot of experimental vs. PSO-predicted IC debonding strength

4. Conclusion

In this study, the aim was to recalibrate an existing analytical model [6] in the literature that estimates the bond strength required to prevent debonding at the NSM-CFRP strip–concrete interface, using the Particle Swarm Optimization (PSO) algorithm. The original structure of the model was preserved. Four different model configurations were evaluated, in which the first two coefficients (K_1 and K_2) were kept constant or considered as optimization parameters. Each configuration was tested through five independent runs under identical PSO settings. Prediction accuracy was evaluated using Root Mean Square Error (RMSE) and Mean Absolute Error (MAE) metrics.

The results show that the PSO-based recalibration improves the predictive performance of the original model, particularly in terms of MAE. The 6.9% reduction in MAE represents a notable improvement in the model's overall consistency. The observed enhancement enables safer and more efficient structural design by reducing the need for excessive material use and improving the accuracy of performance predictions. These findings demonstrate the engineering relevance of the recalibrated model, offering practical benefits in real-world strengthening applications. Scatter plots comparing experimental and predicted loads confirm that the proposed models provide a closer fit to the experimental data. Moreover, the consistent performance across all five trials indicates that the PSO algorithm converged reliably for this specific problem.

The main contribution of this study is to demonstrate the applicability of metaheuristic optimization techniques such as PSO in calibrating bond strength models for NSM CFRP–concrete joints. Without adding complexity to the original model, it was shown that prediction accuracy can be improved by selectively recalibrating specific coefficients and choosing appropriate error metrics. This approach supports more reliable strength estimations, reduces overdesign, and promotes more efficient use of CFRP strips in strengthening applications.

However, the findings of this study are limited by the dataset and interface configuration used. The dataset is relatively small, and the calibration is restricted to specific NSM CFRP–concrete joint configurations. Future studies should aim to include broader datasets encompassing various concrete grades, groove dimensions, and different types and sizes of FRP materials. Additionally, testing other optimization methods or hybrid approaches may further enhance model performance and generalizability.

References

- [1] Ozmen, H. B., & Inel, M. Effect of concrete strength and detailing properties on seismic damage for RC structures. *Res Eng Des.* 2024; 1 (1): 1-11. <http://dx.doi.org/10.17515/rede2024-005en1124rs>
- [2] Sabau, C., Popescu, C., Sas, G., Schmidt, J. W., Blanksvärd, T., & Täljsten, B. (2018). Strengthening of RC beams using bottom and side NSM reinforcement. *Composites Part B: Engineering*, 149, 82-91. <https://doi.org/10.1016/j.compositesb.2018.05.011>
- [3] Sagare, S. S., Kirthiga, R., & Elavenil, S. (2024). A state of art of review on strengthening of concrete structures using fabric reinforced cementitious matrix. *Res. Eng. Struct. Mater.*, 10, 1231-1260. <https://doi.org/10.17515/resm2024.133ma1226rv>
- [4] Al-Saawani, M. A., El-Sayed, A. K., & Al-Negheimish, A. I. (2015). Effect of basic design parameters on IC debonding of CFRP-strengthened shallow RC beams. *Journal of Reinforced Plastics and Composites*, 34(18), 1526-1539. <https://doi.org/10.1177/0731684415593816>
- [5] Li, C., Zhao, Y., Wan, D., Han, X., Li, W., Tian, C., Whag, C., Chang, Z., & Huang, J. (2025). Parameter Analysis for the Flexural Performance of Concrete Beams Using Near-Surface Mounted-Strengthening Application. *Buildings*, 15(9), 1453. <https://doi.org/10.3390/buildings15091453>
- [6] Seracino, R., Raizal Saifulnaz, M. R., & Oehlers, D. J. (2007). Generic debonding resistance of EB and NSM plate-to-concrete joints. *Journal of Composites for Construction*, 11(1), 62-70. [https://doi.org/10.1061/\(ASCE\)1090-0268\(2007\)11:1\(62\)](https://doi.org/10.1061/(ASCE)1090-0268(2007)11:1(62))
- [7] Bianco, V., Barros, J. A., & Monti, G. (2009). Bond model of NSM-FRP strips in the context of the shear strengthening of RC beams. *Journal of Structural Engineering*, 135(6), 619-631. [https://doi.org/10.1061/\(ASCE\)0733-9445\(2009\)135:6\(619\)](https://doi.org/10.1061/(ASCE)0733-9445(2009)135:6(619))
- [8] Zhang, S. S., Ke, Y., Smith, S. T., Zhu, H. P., & Wang, Z. L. (2021). Effect of FRP U-jackets on the behaviour of RC beams strengthened in flexure with NSM CFRP strips. *Composite Structures*, 256, 113095. <https://doi.org/10.1016/j.compstruct.2020.113095>
- [9] Oehlers, D., & Seracino, R. (2004). Design of FRP and steel plated RC structures: Retrofitting beams and slabs for strength, stiffness and ductility. Elsevier.
- [10] Ali, M. M., Oehlers, D. J., Griffith, M. C., & Seracino, R. (2008). Interfacial stress transfer of near surface-mounted FRP-to-concrete joints. *Engineering structures*, 30(7), 1861-1868. <https://doi.org/10.1016/j.engstruct.2007.12.006>
- [11] Seracino, R., Jones, N. M., Ali, M. S., Page, M. W., & Oehlers, D. J. (2007). Bond strength of near-surface mounted FRP strip-to-concrete joints. *Journal of Composites for Construction*, 11(4), 401-409. [https://doi.org/10.1061/\(ASCE\)1090-0268\(2007\)11:4\(401\)](https://doi.org/10.1061/(ASCE)1090-0268(2007)11:4(401))
- [12] Oehlers, D. J., Rashid, R., & Seracino, R. (2008). IC debonding resistance of groups of FRP NSM strips in reinforced concrete beams. *Construction and Building Materials*, 22(7), 1574-1582. <https://doi.org/10.1016/j.conbuildmat.2007.03.021>
- [13] Oehlers, D. J., Haskett, M., Wu, C., & Seracino, R. (2008). Embedding NSM FRP plates for improved IC debonding resistance. *Journal of Composites for Construction*, 12(6), 635-642. [https://doi.org/10.1061/\(ASCE\)1090-0268\(2008\)12:6\(635\)](https://doi.org/10.1061/(ASCE)1090-0268(2008)12:6(635))
- [14] Rashid, R., Oehlers, D. J., & Seracino, R. (2008). IC debonding of FRP NSM and EB retrofitted concrete: plate and cover interaction tests. *Journal of Composites for Construction*, 12(2), 160-167. [https://doi.org/10.1061/\(ASCE\)1090-0268\(2008\)12:2\(160\)](https://doi.org/10.1061/(ASCE)1090-0268(2008)12:2(160))
- [15] Zhang, S. S., Teng, J. G., & Yu, T. (2014). Bond strength model for CFRP strips near-surface mounted to concrete. *Journal of Composites for Construction*, 18(3), A4014003. [https://doi.org/10.1061/\(ASCE\)CC.1943-5614.0000402](https://doi.org/10.1061/(ASCE)CC.1943-5614.0000402)
- [16] Bilotta, A., Ceroni, F., Nigro, E., & Pecce, M. (2015). Efficiency of CFRP NSM strips and EBR plates for flexural strengthening of RC beams and loading pattern influence. *Composite Structures*, 124, 163-175. <https://doi.org/10.1016/j.compstruct.2014.12.046>
- [17] D'Antino, T., & Pisani, M. A. (2020). General analytical model for the bond capacity of NSM FRP-concrete joints. *Journal of Composites for Construction*, 24(6), 04020065. [https://doi.org/10.1061/\(ASCE\)CC.1943-5614.0001076](https://doi.org/10.1061/(ASCE)CC.1943-5614.0001076)
- [18] Naderpour, H., Mirrashid, M., & Nagai, K. (2020). An innovative approach for bond strength modeling in FRP strip-to-concrete joints using adaptive neuro-fuzzy inference system. *Engineering with computers*, 36(3), 1083-1100. <https://doi.org/10.1007/s00366-019-00751-y>
- [19] Milovancevic, M., Denić, N., Ćirković, B., Nešić, Z., Paunović, M., & Stojanović, J. (2021). Prediction of shear debonding strength of concrete structure with high-performance fiber reinforced concrete. *Structures*, 33, 4475-4480. <https://doi.org/10.1016/j.istruc.2021.07.012>
- [20] Kumar, A., Arora, H. C., Kumar, K., Garg, H., & Jahangir, H. (2024). Development of efficient prediction model of FRP-to-concrete bond strength using curve fitting and ANFIS methods. *Arabian Journal for Science and Engineering*, 49(4), 5129-5158. <https://doi.org/10.1007/s13369-023-08328-0>

- [21] Poonam, S. V. (2024). Response surface methodology use in optimization of concrete properties using blast furnace slag aggregate and recycled concrete sand. *Res. Eng. Struct. Mater*, 10(1), 111-133. <https://doi.org/10.17515/resm2023.788me0614>
- [22] Sharma, K. K., Imam, A., Anifowose, F., & Srivastava, V. (2020). Compressive strength modeling of blended concrete based on empirical and artificial neural network techniques. *Journal of structural integrity and maintenance*, 5(4), 252-264. <https://doi.org/10.1080/24705314.2020.1783120>
- [23] Imam, A., Salami, B. A., & Oyehan, T. A. (2021). Predicting the compressive strength of a quaternary blend concrete using Bayesian regularized neural network. *Journal of Structural Integrity and Maintenance*, 6(4), 237-246. <https://doi.org/10.1080/24705314.2021.1892572>
- [24] Mohamed, O., Kewalramani, M., Ati, M., & Al Hawat, W. (2021). Application of ANN for prediction of chloride penetration resistance and concrete compressive strength. *Materialia*, 17, 101123. <https://doi.org/10.1016/j.mtla.2021.101123>
- [25] Ebid, A. M., & Deifalla, A. (2021). Prediction of shear strength of FRP reinforced beams with and without stirrups using (GP) technique. *Ain Shams Engineering Journal*, 12(3), 2493-2510. <https://doi.org/10.1016/j.asej.2021.02.006>
- [26] Zhang, S. Y., Chen, S. Z., Jiang, X., & Han, W. S. (2022). Data-driven prediction of FRP strengthened reinforced concrete beam capacity based on interpretable ensemble learning algorithms. *Structures*, 43, 860-877. <https://doi.org/10.1016/j.istruc.2022.07.025>
- [27] Al-Hamrani, A., Wakjira, T. G., Alnahhal, W., & Ebead, U. (2023). Sensitivity analysis and genetic algorithm-based shear capacity model for basalt FRC one-way slabs reinforced with BFRP bars. *Composite Structures*, 305, 116473. <https://doi.org/10.1016/j.compstruct.2022.116473>
- [28] Baji, H., Yang, W., & Li, C. Q. (2018). Optimal FRP-strengthening strategy for corrosion-affected reinforced concrete columns. *Structure and Infrastructure Engineering*, 14(12), 1586-1597. <https://doi.org/10.1080/15732479.2018.1476560>
- [29] Mahdavi, G., Nasrollahzadeh, K., & Hariri-Ardebili, M. A. (2019). Optimal FRP jacket placement in RC frame structures towards a resilient seismic design. *Sustainability*, 11(24), 6985. <https://doi.org/10.3390/su11246985>
- [30] Li, G., Hu, T., & Bai, D. (2021). BP Neural Network Improved by Sparrow Search Algorithm in Predicting Debonding Strain of FRP-Strengthened RC Beams. *Advances in Civil Engineering*, 2021(1), 9979028. <https://doi.org/10.1155/2021/9979028>
- [31] Hu, T., Wang, J., Li, G., & Zheng, B. (2021). Prediction of Allowable Debonding Strain of FRP-Strengthened RC Beam Based on GA-BP Neural Network. *IOP Conference Series: Earth and Environmental Science*, 719(2), 022028. <https://doi.org/10.1088/1755-1315/719/2/022028>
- [32] Ghaidan, D. J., Mohammed, H. J., & Salahaldin, A. I. (2024). Predicting Failure Modes of RC Beams Strengthening with FRP-NSM System: A Statistical Approach. *International Journal of Sustainable Construction Engineering and Technology*, 15(1), 226-240. <https://doi.org/10.30880/ijscet.2024.15.01.016>
- [33] Jiang, W., Xie, Y., Li, W., Wu, J., & Long, G. (2021). Prediction of the splitting tensile strength of the bonding interface by combining the support vector machine with the particle swarm optimization algorithm. *Engineering Structures*, 230, 111696. <https://doi.org/10.1016/j.engstruct.2020.111696>
- [34] Ji, W., Qin, Y., Liu, J., Zhang, X., & Zhou, H. (2025). Parameter inverse of fiber-cement matrix interface cohesive model based on PSO algorithm. *Structural Concrete*. <https://doi.org/10.1002/suco.70148>
- [35] Ghodousian, O., Garcia, R., Shafaie, V., & Ghodousian, A. (2023). Interfacial bond strength of coloured SCC repair layers: an experimental and optimisation study. *Journal of Structural Integrity and Maintenance*, 8(3), 140-149. <https://doi.org/10.1080/24705314.2023.2170620>
- [36] Mohammadizadeh, M. R., & Esfandnia, F. (2022). Predicting Compression Strength of Reinforced Concrete Columns Confined by FRP Using Meta-Heuristic Methods. *Civil Engineering Infrastructures Journal*, 55(1), 1-17. <https://doi.org/10.22059/cej.2021.304229.1685>
- [37] Wahab, S., Suleiman, M., Shabbir, F., Mahmoudabadi, N. S., Waqas, S., Herl, N., & Ahmad, A. (2023). Predicting confinement effect of carbon fiber reinforced polymers on strength of concrete using metaheuristics-based artificial neural networks. *arXiv preprint arXiv:2403.13809*. <https://doi.org/10.48550/arXiv.2403.13809>
- [38] Nguyen, T. A., & Lý, H. B. (2021). Estimation of the bond strength between FRP and concrete using ANFIS and hybridized ANFIS machine learning models. *Journal of Science and Transport Technology*, 34-44. <https://doi.org/10.58845/jstt.utt.2021.en.1.1.34-44>
- [39] Su, M., Peng, H., & Li, S. F. (2021). Application of an interpretable artificial neural network to predict the interface strength of a near-surface mounted fiber-reinforced polymer to concrete joint. *Journal of Zhejiang University-SCIENCE A*, 22(6), 427-440. <https://doi.org/10.1631/jzus.A2000245>
- [40] Kumar, A., Arora, H. C., Mohammed, M. A., Kumar, K., & Nedoma, J. (2021). An optimized neuro-bee algorithm approach to predict the FRP-concrete bond strength of RC beams. *IEEE Access*, 10, 3790-3806. <https://doi.org/10.1109/ACCESS.2021.3140046>

- [41] Kumar, A., Arora, H. C., Kapoor, N. R., & Kumar, A. (2024). Artificial neural network optimized with PSO to estimate the interfacial properties between FRP and concrete surface. *Advances in Computers*, 135, 497-527. <https://doi.org/10.1016/bs.adcom.2023.11.014>
- [42] Pei, Z., & Wei, Y. (2022). Prediction of the bond strength of FRP-to-concrete under direct tension by ACO-based ANFIS approach. *Composite Structures*, 282, 115070. <https://doi.org/10.1016/j.compstruct.2021.115070>
- [43] Zhang, F., Wang, C., Liu, J., Zou, X., Sneed, L. H., Bao, Y., & Wang, L. (2023). Prediction of FRP-concrete interfacial bond strength based on machine learning. *Engineering structures*, 274, 115156. <https://doi.org/10.1016/j.engstruct.2022.115156>
- [44] Tao, L., & Xue, X. (2024). An improved random forest model to predict bond strength of FRP-to-concrete. *Journal of Civil Engineering and Management*, 30(6), 520-535. <https://doi.org/10.3846/jcem.2024.21636>
- [45] Shbeeb, N. I., Katash, A. A., Oğuzmert, M., & Barham, W. S. (2024). Estimation of the bond strength of fiber-reinforced polymer bars in concrete using artificial intelligence systems. *Buildings*, 14(2), 369. <https://doi.org/10.3390/buildings14020369>
- [46] Xue, X., Zhang, R., Chen, X., & Tao, L. (2024). Bond strength prediction of FRP reinforced concrete using soft computing techniques: X. Xue et al. *Soft Computing*, 28(19), 11553-11564. <https://doi.org/10.1007/s00500-024-09904-8>
- [47] Haddad, R., Almasaeid, H., & Saeed, A. (2026). Predicting Bond Strength between Externally Bonded FRP and Heat-damaged Concrete Using ANN. *Journal of Soft Computing in Civil Engineering*, 10(1), e223688. <https://doi.org/10.22115/scce.2025.1945>
- [48] Kennedy, J., & Eberhart, R. (1995). Particle Swarm Optimization. *Proceedings of ICNN'95-International Conference on Neural Networks*, 4, 1942-1948. <https://doi.org/10.1109/ICNN.1995.488968>
- [49] Çevik, K., & Koçer, H. (2013). A Soft Computing Application Based On Artificial Neural Networks Training by ParticleSwarm Optimization. *Süleyman Demirel University Journal of Natural and Applied Sciences*, 17(2), 39-45.
- [50] Derdiman, M. K. (2022). Reliability-Based Cross-Section Optimization of Cantilever Slabs Using Discrete PSO Algorithm. *Journal of Engineering Sciences and Design*, 10(3), 987-999. <https://doi.org/10.21923/jesd.952838>
- [51] Saphioğlu, K. (2025). Calibration of Linear Muskingum Model Coefficients and Coefficient Parameters Using Grey Wolf and Particle Swarm Optimization. *Water Resources Management*, 39(3), 999-1014. <https://doi.org/10.1007/s11269-024-04063-9>
- [52] Özsağlam, M. Y., & Çunkaş, M. (2008). Particle Swarm Optimization Algorithm for Solving Optimization Problems. *Journal of Polytechnic*, 11(4), 299-305.
- [53] Saphioğlu, K., Öztürk, T. S. K., & Acar, R. (2020). Optimization of open channels using particle swarm optimization algorithm. *Journal of Intelligent & Fuzzy Systems*, 39(1), 399-405. <https://doi.org/10.3233/JIFS-191355>
- [54] Yazd, H. G. H., Arabshahi, S. J., Tavousi, M., & Alvani, A. (2015). Optimal designing of concrete gravity Dam using particle swarm optimization algorithm (PSO). *Indian Journal of Science and Technology*, 8(12), 1. <https://doi.org/10.17485/ijst/2015/v8i12/70714>